Received: 23 August 2024 | Revised: 14 January 2025 | Accepted: 31 January 2025

DOI: 10.1002/mrm.30469

RESEARCH ARTICLE

Magnetic Resonance in Medicine

Free-running 5D whole-heart MRI for isotropic cardiac function measurements at 3T without contrast agents

Augustin C. Ogier[1] | **Isabel Montón Quesada**[1] | **Xavier Sieber**[1] | **Pauline Calarnou**[1] | **Jean-Baptiste Ledoux**[1,2] | **Bastien Milani**[1] | **Panagiotis Antiochos**[3] | **Juerg Schwitter**[3] | **Christopher W. Roy**[1] | **Jérôme Yerly**[1,2] | **Matthias Stuber**[1,2] | **Ruud B. van Heeswijk**[1]

[1]Department of Radiology, Lausanne University Hospital (CHUV) and University of Lausanne (UNIL), Lausanne, Switzerland

[2]CIBM Center for Biomedical Imaging (CIBM), Lausanne, Switzerland

[3]Heart and Vessel Department, Lausanne University Hospital (CHUV) and University of Lausanne (UNIL), Lausanne, Switzerland

Correspondence
Ruud B. van Heeswijk, Department of Radiology, Lausanne University Hospital (CHUV) and University of Lausanne (UNIL), CIBM-CHUV, Rue de Bugnon 46, BH 8.84, 1011 Lausanne, Switzerland
Email: ruud.mri@gmail.com

Funding information
Swiss National Science Foundation, Grant/Award Number: FF23129; Swiss Heart Foundation, Grant/Award Numbers: 320030B_201292, 320030_173129, 32003B_182615, 326030_150828, PZ00P3_202140, RSII5_202276

Abstract

Purpose: To optimize and characterize an interrupted 5D free-running framework at 3 T for detailed cardiac function assessment without the use of breath holding or contrast agents.

Methods: A free-running 3D radial gradient echo sequence was periodically interrupted with a T_2 preparation and a recovery module to optimize native blood-to-myocardium contrast at 3 T. Lipid signal was suppressed using a numerically optimized water-excitation RF pulse to reduce lipid streaking artifacts and to improve overall image quality. Optimal acquisition parameters were established for a 5-min scan time using extended phase graph simulations. A compressed sensing-based reconstruction incorporating cardiac and respiratory inter-bin deformation fields was employed to generate 5D images of the whole heart. The sharpness and contrast between the left ventricular blood pool and myocardium, along with the functional measurements of the left ventricle from the 5D datasets, were compared to routine 2D cine imaging in 16 healthy volunteers and three patients referred for clinically indicated CMR.

Results: The proposed method resulted in lower contrast (0.57 ± 0.12 vs. 2.09 ± 0.74, $p < 0.001$) and sharpness (3.76 ± 1.11 mm vs. 2.74 ± 0.95 mm, $p < 0.001$), but enabled similar left-ventricle ejection fraction assessment (bias = 1.3%, limits of agreement = [−3.3%, 5.9%], intraclass correlation coefficient = 0.87, $p = 0.03$) with high reproducibility compared to 2D cine.

Conclusion: The proposed contrast-free, interrupted free-running 5D imaging provides left ventricular functional assessments comparable to 2D cine at 3 T, while offering an improved patient experience through shorter scan times and free breathing.

KEYWORDS

3T, 5D whole-heart MRI, compressed sensing, contrast-agent-free, free-running, non-rigid motion correction, T_2 preparation pulse

1 | INTRODUCTION

Cardiovascular disease (CVD) remains the foremost cause of morbidity and mortality worldwide.[1] In most CVDs, the left ventricle in particular undergoes several modifications that impact its anatomy and function.[2] To quantify these changes, cardiovascular magnetic resonance (CMR) imaging is routinely used, typically using 2D balanced steady-state free precession (bSSFP) cine imaging.[3,4] This technique, while effective, requires reliable ECG signals, repetitive breath-holds, and precise planning of cardiac views, resulting in prolonged scan times and necessitating specialized technologists. Moreover, these methods can be challenging for certain patients to tolerate.

Recent advances have introduced free-running (FR) acquisitions for continuous whole-heart imaging, eliminating the need for breath holding and ECG triggering.[5,6] These approaches continuously capture data, allowing for the retrospective extraction of respiratory signals from the raw data,[7] while cardiac signals are obtained through either self-gating[5,8] or ECG monitoring.[6] When combined with compressed sensing image reconstruction, such methods enable the generation of isotropic high-temporal-resolution 5D images.[9] This enables a comprehensive 3D view of the whole heart through cardiac and respiratory motion states, allowing for retrospective reformatting in any orientation. These advantages enhance workflow efficiency and reduce operator dependency, as they eliminate the need for predefined scan plane orientations and breath-holds.

5D FR acquisitions have initially been designed for 1.5 T using bSSFP-based pulse sequences.[9] Many cardiac imaging centers primarily use 3 T MRI scanners, which are often preferred due to their superior performance in various organ systems. Despite their increasing prevalence, 3 T MRI systems present distinct challenges compared to 1.5 T systems, especially in the heart. At 3 T, spoiled gradient-recalled echo (GRE) sequences are often preferred due to their robustness against magnetic field inhomogeneities and their lower specific absorption rate (SAR) compared to bSSFP sequences.[10] However, GRE imaging inherently offers poor contrast between the myocardium and the blood pool, necessitating the use of contrast agents in FR acquisitions to enhance image quality and to enable accurate cardiac function assessment.[5,11]

Although gadolinium-based contrast agents have a well-established safety profile and are widely used, there are remaining concerns about their long-term retention in tissues after multiple examinations,[12] even though there is no evidence of toxicity in modern formulations.[13] There is therefore still a drive for MRI without contrast agents, as gadolinium-free imaging can be performed in patients with severe kidney failure as well as pregnant and lactating women. Additionally, non-contrast examinations lower costs and streamline clinical workflows, making the process faster, less expensive, and less invasive.

Based on the longer T_2 relaxation time of blood compared to the myocardium and surrounding tissues, T_2 preparation (T_2 prep) modules are commonly used in non-contrast CMR to enhance blood-to-myocardium contrast.[14,15] When combined with fat saturation pulses, which minimize the high signal from fat and reduce lipid streaking artifacts, these techniques are particularly effective for whole-heart MR coronary angiography.[16–20] Utilizing respiratory navigators and ECG-gating methods, these approaches generate high-resolution static 3D images that, however, do not allow for the assessment of cardiac function over time.

In this study, we therefore optimize and characterize an interrupted free-running (IFR) GRE pulse sequence for detailed cardiac function assessment at 3 T without the use of contrast agents. Adiabatic T_2 prep[21] and recovery time modules were integrated into a GRE FR acquisition to enhance blood-to-myocardium contrast. To reduce lipid streaking artifacts and improve overall image quality, the lipid signal was suppressed using a numerically optimized water-excitation RF pulse.[22] An optimal set of acquisition parameters was determined using extended phase graph (EPG) simulations to ensure the highest native blood-to-myocardium contrast. The proposed framework was compared to and validated against a clinical reference standard 2D cine acquisition, using metrics related to cardiac function and image quality.

2 | METHODS

2.1 | Estimation of optimal IFR acquisition parameters

An IFR GRE sequence was designed by integrating T_2 prep and recovery time modules to enhance the contrast between the blood pool and the myocardium. The proposed sequence is thus made up of successive blocks composed of a T_2 prep module followed by readouts arranged in a 3D golden angle phyllotaxis radial trajectory,[23] and then a magnetization recovery time. This 3D radial trajectory has the advantage that all readouts traverse *k*-space from the periphery through the center and back out to the periphery, ensuring that all magnetization changes equally apply for the *k*-space center and periphery. Several parameters of the IFR pulse sequence influence the blood-to-myocardium contrast and need to be optimized. The main parameters impacting this contrast are the RF excitation angle (α), the adiabatic T_2 prep echo time (TE_{T_2p}), the recovery time duration (T_{rec}),

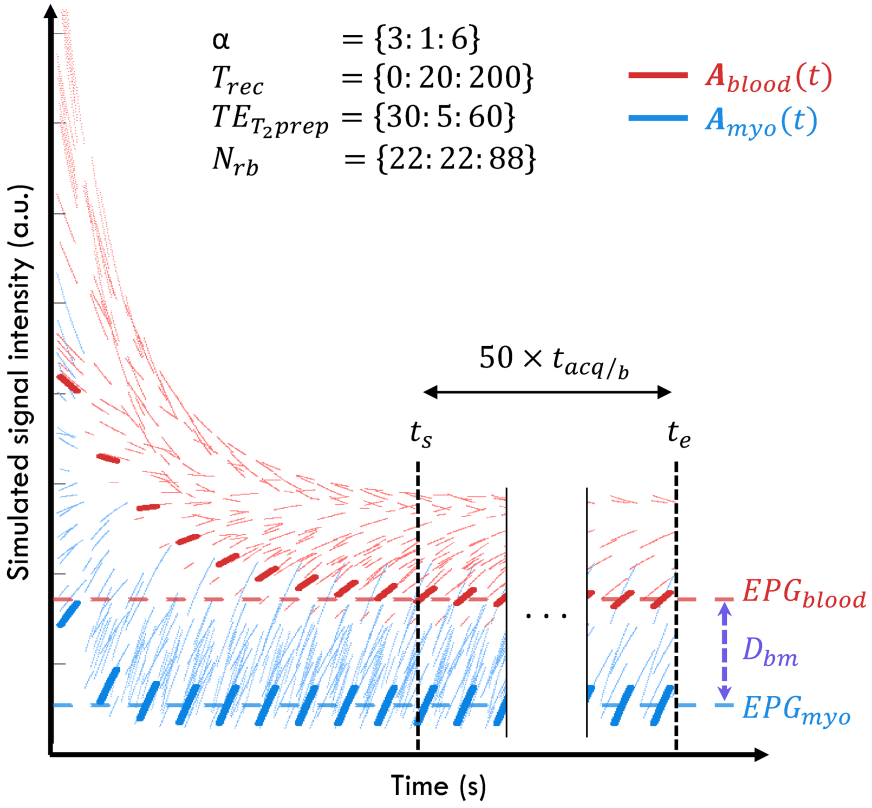

FIGURE 1 Extended phase graph (EPG) simulations were conducted to optimize the blood-myocardium contrast. The different sets of parameters resulted in varying theoretical signal intensities of the blood (A_{blood}) and myocardium (A_{myo}), which were computed at the center of each echo and are represented by discrete points. Theoretical blood-to-myocardium signal differences (D_{bm}) were calculated as the average signal intensity difference between the two tissues, using the signal intensities at the center of each echo within the interrupted steady state from t_s to t_e. The sequence parameters that were varied in the simulations were: $t_{acq/b}$ = duration of an acquisition block, α = RF excitation angle, T_{rec} = recovery time duration, TE_{T_2p} = T_2 prep duration, N_{rb} = number of readouts per T2 prep.

and the number of readouts per acquisition block (N_{rb}) (i.e. per T_2 prep). The optimal set of these parameters was determined with EPG simulations.[24] Magnetization behavior has been investigated for a multitude of combinations of the abovementioned parameters to determine those that result in the highest contrast, that is, the largest difference between the signals of the blood pool and the myocardium (Figure 1). The theoretical difference of signal intensity (D_{bm}) between those two tissues can be formulated as:

$$D_{bm}\left(\alpha, T_{\text{rec}}, TE_{T_2p}, N_{rb}\right) = EPG\left(T_{1_{blood}}, T_{2_{blood}}\right) - EPG\left(T_{1_{myo}}, T_{2_{myo}}\right), \quad (1)$$

with

$$EPG\left(T_1, T_2\right) = \frac{1}{N_t}\sum_{n=1}^{N_t} \boldsymbol{A}\left[\alpha, T_{\text{rec}}, TE_{T_2p}, N_{rb}, T_1, T_2\right](t_n), \quad (2)$$

where $\boldsymbol{A}[\cdots](t)$ denotes the signal intensity computed by EPG at each readout time-point t, based on the specified sequence parameters and tissue relaxometry properties, N_t the number of readouts over which $\boldsymbol{A}(t)$ is evaluated, and $t_n \in [t_s, t_e]$. The choice of t_s ensures that the system has reached its interrupted steady state, typically achieved within a few seconds, while t_e is chosen to allow enough time for precise averaging of the estimated signal intensity. In practice, t_s was determined as the time where the maximum signal amplitude stabilized within ±0.1% across two successive acquisition blocks and t_e as t_s plus the duration necessary to complete the acquisition of 50 blocks. T_1/T_2 values of 1470/47 ms for the myocardium and 1930/275 ms for the blood pool were used.[25] Increasing the duration of some parameters such as TE_{T_2p} or T_{rec} typically enhances contrast but simultaneously extends the acquisition time considerably. Given a repetition time (TR), the duration of an acquisition block ($t_{acq/b}$) is:

$$t_{acq/b}\left(T_{\text{rec}}, TE_{T_2p}, N_{rb}\right) = TE_{T_2p} + (N_{rb} \cdot TR) + T_{\text{rec}}. \quad (3)$$

The total acquisition time of the sequence (t_{acq}) is then given by:

$$t_{\text{acq}}\left(T_{\text{rec}}, TE_{T_2p}, N_{rb}\right) = N_{rt}/N_{rb} \cdot t_{acq/b}, \quad (4)$$

where N_{rt} denotes the total number of readouts in the acquisition, a global constant that can be estimated based on the Nyquist percentage required for the intended application, which is primarily determined by the desired image resolution and the number of cardiac and respiratory phases. The optimization problem can finally be formulated as follows:

$$\underset{\substack{\alpha \\ T_{\text{rec}} \\ TE_{T_2p} \\ N_{rb}}}{\operatorname{argmax}} \left[D_{bm}(\alpha, T_{\text{rec}}, TE_{T_2p}, N_{rb}) \right]$$

$$\text{s.t.} \quad \begin{cases} \alpha \in \Omega_{\alpha}(3,1,6) \\ T_{\text{rec}} \in \Omega_{T_{\text{rec}}}(0,20,200) \\ TE_{T_2p} \in \Omega_{TE_{T_2p}}(30,5,60), \\ N_{rb} \in \Omega_{N_{rb}}(22,22,88) \\ t_{\text{acq}}\left(T_{\text{rec}}, TE_{T_2p}, N_{rb}\right) \end{cases} \tag{5}$$

where Ω_x denotes the set of simulated parameters such as $\Omega_x(l, \Delta, m) = \{x_n = l + n \cdot \Delta \mid n = 0, 1, \ldots, [(m-l)/\Delta]\}$. In this study, the sets of parameter values considered were $\Omega_{\alpha}(3,1,6)$, $\Omega_{T_{\text{rec}}}(0,20,200)$, $\Omega_{TE_{T_2p}}(30,5,60)$, and $\Omega_{N_{rb}}(22,22,88)$. It should be noted that the N_{rb} readouts used in this EPG simulation framework could be distributed across several consecutive interleaves of the radial trajectory with a phyllotaxis pattern, such that adequate k-space sampling uniformity after the data binning can be ensured for the CS-based reconstruction detailed later. These parameter sets are compared for a user-defined acquisition time. A longer t_{acq} allows for greater theoretical contrast. Simulations without T_2 prep were also conducted.

In this study, an isotropic resolution of $1.96 \times 1.96 \times 1.96$ mm^3 and a field of view of $220 \times 220 \times 220$ mm^3 were selected to accurately distinguish the endocardial contours. The acquisition time was set to 5 min as it fit within the clinical protocol and was considered a practical and reasonable duration for clinical use.

Considering four respiratory bins and an average heart rate of 70 beats per minute, resulting in 18 cardiac bins, 45,276 radial readouts were required throughout the acquisition to achieve a Nyquist percentage of about 3.2% per motion state bin for the selected isotropic resolution of (1.96 mm)^3. The IFR sequence parameters were simulated using EPG for these 45,276 readouts and a scan duration of approximately 4 to 6 min. This extended simulation duration, beyond the intended 5-min acquisition time, was used to thoroughly characterize the behavior of the various parameters and to minimize the risk of selecting a local minimum.

2.2 | Acquisition protocol

Acquisitions were performed in 16 healthy volunteers (10F, 33.7 ± 10.7y) and three patients (1F 39y, 1M 68y, 1M 24y) clinically referred for CMR on a 3 T clinical scanner (Magnetom PrismaFit for the healthy volunteers and Magnetom VidaFit for the patients, both Siemens Healthineers, Erlangen, Germany). The three patients were diagnosed with ventricular extrasystoles (F, 39y), Fabry disease (M, 24y), and chronic ischemic heart disease with evidence of intracavitary thrombus (F, 68y). The study was approved by the institutional review board, and written informed consent was obtained from all participants prior to MR scanning.

To reduce streaking artifacts due to bright signals from fat and thus to enhance image quality, the proposed IFR GRE sequence (Figure 2) used a B-spline interpolated water-excitation RF pulse[22] with a 1 ms pulse duration. This water-excitation RF pulse provides an efficient alternative to fat saturation pulses, which are less suitable for radial acquisitions where each readout passes through the center of *k*-space. Each consecutive interleave of the 3D radial trajectory was initiated by a readout oriented in the superior–inferior (SI) direction for the extraction of cardiac and respiratory motion signals.[5,9]

In five healthy subjects, an FR GRE acquisition was performed without T_2 preparation and recovery time modules to demonstrate the absence of blood-to-myocardium contrast. EPG simulations, similar to those used for the proposed IFR sequence, were conducted to optimize the flip angle. To ensure consistency with the IFR sequence, the total number of readouts and N_{rb} were fixed, preserving the same phyllotaxis pattern and undersampling. For both sequences, a repetition time of 3:50 ms was employed.

The scan efficiency (i.e., what percentage of time the ADC is open relative to the total scan duration) was calculated for the optimized IFR sequence as well as for the continuously acquired FR sequence without T_2 or recovery modules.

A stack of 2D short-axis (SAX) bSSFP cine images was acquired, along with single-slice two-chamber and four-chamber views, for comparison with the proposed IFR sequence. The sequence parameters were TE = 1.5 ms, TR = 3.4 ms, RF excitation angle of 47°, 1.4×1.4 mm^2 in-plane resolution, 8 mm slice thickness, 2 mm slice gap, compressed sensing factor of 8.6, and a receiver bandwidth of 977 Hz/pixel.[26,27] All 2D cine images were acquired using repetitive end-expiratory breath-holds of approximately 10 s interspersed with respiratory recovery periods of at least 15 s and were reconstructed to 25 phases according to the clinical reference protocol.

All acquisitions were performed with a 34-channel chest-spine coil array, of which the signal of the 24 closest elements to the field of view was retained. A pulse oximeter was placed on the subjects' index finger to monitor the heart rate in real time throughout the acquisition. In the patients, the heart rate was monitored by ECG.

2.3 | Motion extraction

SI projections computed as the one-dimensional Fourier transform of SI readouts were used for cardiac and

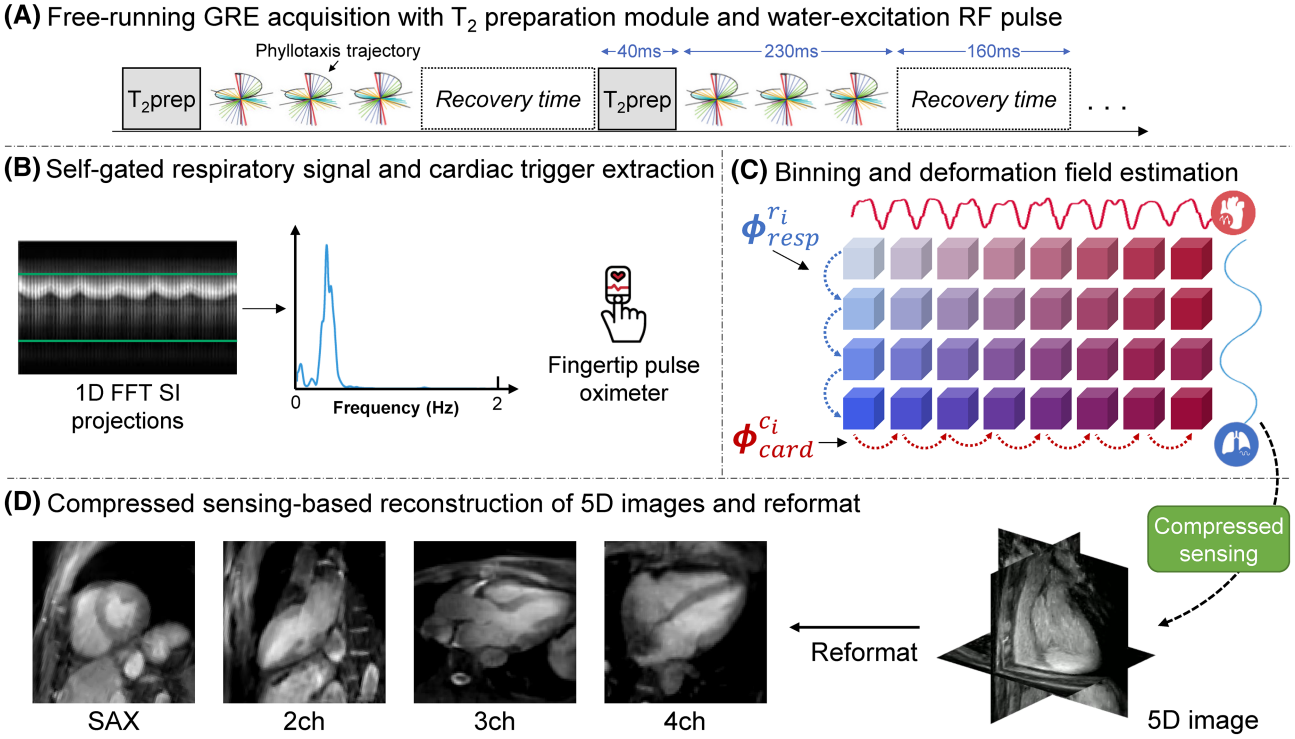

FIGURE 2 Schematic overview of the acquisition and reconstruction framework. A free-running GRE sequence is used with a 3D golden-angle phyllotaxis radial trajectory and a numerically optimized water-excitation RF pulse and is interrupted with T_2 prep and recovery time modules to generate contrast between the blood and the myocardium (A). The respiratory self-gating signal, extracted from the central half of the superior–inferior (SI) projections, and the cardiac signature, obtained using a pulse oximeter (B), are used to bin the data. This binned data enters compressed-sensing-based reconstruction pipeline that includes deformation fields to compensate for inter-bin motion (C). The generated 5D image can be retrospectively reformatted in any desired 2D view (D).

respiratory self-gating signal extraction in FR acquisitions.[5,9] Due to the T_2 prep module, the magnetization systematically differs between the SI projection of a same acquisition block in the proposed IFR sequence. To mitigate artifacts stemming from this intensity change, only the first SI projection of each acquisition block was considered. Additionally, only the central half of the SI projection was used, as the periphery contains minimal pertinent physiological motion data; specifically, the top quarter corresponds to the neck, while the bottom quarter is in the abdomen; both do not contribute effectively to cardiac or respiratory motion retrieval. The SI data from each receiver coil element were concatenated to form a 2D matrix $\boldsymbol{S}$ of size $1/2 \cdot N_p \cdot N_c$ by N_{rt}/N_{rb} with N_p the number of k-space samples in a readout, and N_c the number of coil elements. An angular dependence correction was then applied to this matrix to eliminate trajectory-related effects induced by the pseudo-periodic sampling trajectory and eddy currents.[9] The matrix $\boldsymbol{S}$ links a vector of size $1/2 \cdot N_p \cdot N_c$ to each time t corresponding to the acquisition of the first SI readout of each acquisition block (Figure 2B).

A principal component analysis (PCA) was applied to $\boldsymbol{S}$ along the $(1/2 \cdot N_p \cdot N_c)$ dimension to project the data in a lower dimensional space to simplify its analysis and to reduce the computation costs. The respiratory signal was automatically identified by selecting the PCA score $\boldsymbol{w}_i\boldsymbol{S}$, with i given by:

$$\underset{i\in[1,N_w]}{\operatorname{argmax}}\left[\max_{j\in[1,N_{g_i}]}\left(a_{ij}\sum_{f=f_s}^{f_e}e^{-\left(\frac{f-b_{ij}}{2}\right)^2}\Big/\sum_{f=f_s}^{f_e}\hat{\boldsymbol{s}}_i(f)\right)\right], \quad (6)$$

where $\hat{\boldsymbol{s}}_i$ is the power spectral density of $\boldsymbol{w}_i\boldsymbol{S}$, N_w the number of PCA coefficients calculated, N_{g_i} the number of Gaussian models fitted on $\hat{\boldsymbol{s}}_i$, a and b the amplitude and centroid location of each Gaussian fit, and $[f_s, f_e]$ the frequency window selected to span a reasonable range of physiological motion frequencies.

In practice, N_w was set to 10, and N_{gi} was set to the number of local maxima in $\hat{\boldsymbol{s}}_i$ with a prominence of at least one tenth of the maximum value inside the $[f_s, f_e]$ frequency range. For the respiratory signal, the range of $f_s = 0.05$ Hz and $f_e = 0.7$ Hz was used.

This formulation favors signals with a fundamental frequency inside of the expected physiological range and also disfavors signals with spurious peaks inside of this range. Quasi-periodic physiological motions, such as respiratory motion, are expected to have only one principal component with a normal distribution. As

several components can embed the same physiological motion, the ratio between the integral of the Gaussian fit and the integral of $\hat{\boldsymbol{s}}_i$ was weighted by the maximum amplitude of the Gaussian fit to retain the component with the strongest signal.

Such an approach relies on a sufficiently high temporal sampling of SI readouts in $\boldsymbol{S}$ to capture the desired physiological motion. Although this is respected for the respiratory signal, the additional T_2 prep and recovery time modules introduced in our IFR acquisition, as well as the T_2 prep interference between the SI readouts of the same acquisition block, do not always allow sufficient SI readout sampling to adequately capture cardiac motion. Cardiac signatures were therefore recovered using multi-scale peak and trough detection[28] on the recorded pulse oximeter signal. The pulse oximeter was used instead of ECG to avoid the deleterious effects of gradient switching and the magnetohydrodynamic effect on the ECG signal, which are relatively strong for fast spoiled gradient echo sequences at 3 T. As a last processing step, the respiratory signal $\boldsymbol{w}_i\boldsymbol{S}$ was refined using a narrow low-pass Butterworth filter to reject potential artifacts at higher frequencies than 0.7 Hz.

2.4 | 5D image reconstruction

The cardiac signature from the pulse oximeter and the self-gated respiratory signal were used to bin the acquired data into cardiac and respiratory phases, yielding undersampled 5D data. Binning in the respiratory dimension was performed by dividing the respiratory signal into four equally populated phases ranging from end-expiration to end-inspiration. The cardiac signature was used to sort the data in non-overlapping phases of 50 ms. To confirm that the sampling pattern results in sufficient data per cardiac and respiratory motion state, the amount of samples per motion state was quantified for each participant as a percentage of the radial Nyquist criterion given by $N_{\mathrm{rt}} \Big/ \left(\frac{1}{4} \cdot \pi \cdot N_p\right)$.

The potential risk of over-regularization in the reconstruction of motion-resolved cardiac images, particularly in non-contrast enhancement acquisitions, has been recently highlighted.[29] The diminished contrast of GRE sequences at 3 T may result in increased susceptibility to motion artifacts when higher regularization is applied in CS-based reconstruction techniques. To mitigate potential motion compression in CS-based reconstruction of FR data, several methods have been recently proposed that incorporate deformation fields computed between cardiac[29–31] or respiratory[32,33] bins. Such approaches allow the use of larger regularization weights to mitigate artifacts without introducing motion blur. In this study, we integrated both cardiac and respiratory inter-bin deformation fields into CS-based reconstruction (Figure 2C) to reduce sensitivity to user-defined parameters, thereby theoretically improving both the quality of reconstructed images and the fidelity of motion representation.

Building upon the established FR reconstruction framework,[9,34] the proposed framework integrated both cardiac and respiratory inter-bin deformation fields within the k-t sparse SENSE reconstruction of the highly undersampled 5D images. We consider cardiac (c) and respiratory (r) motion-resolved 3D images $\boldsymbol{x}_{r,c}$ reconstructed from k-space data $\boldsymbol{y}_{r,c}$ that is sorted into n_c cardiac bins and n_r respiratory bins. The rearranged optimization problem can be expressed as:

$$\begin{aligned}\hat{\boldsymbol{x}} = \underset{\boldsymbol{x}\in X}{\operatorname{argmin}}\Big(&\frac{1}{2}\Sigma_{c=1}^{n_c}\Sigma_{r=1}^{n_r}\|\boldsymbol{A}_{r,c}\boldsymbol{x}_{r,c}-\boldsymbol{y}_{r,c}\|_2^2\\ &+\lambda_C\Sigma_{c=1}^{n_c}\|\nabla_C^f\boldsymbol{x}_{r,c}\|_1\\ &+\lambda_R\Sigma_{r=1}^{n_r}\|\nabla_R^f\boldsymbol{x}_{r,c}\|_1\\ &+\lambda_R\Sigma_{r=1}^{n_r}\|\nabla_R^b\boldsymbol{x}_{r,c}\|_1\Big),\end{aligned} \tag{7}$$

where $\boldsymbol{A}_{r,c}$ combines the non-uniform Fourier transform and coil sensitivity for each cardiac and respiratory frame. The forward (f) and backward (b) operators[32] applying the first-order difference between the cardiac (C) and respiratory (R) dimensions while taking into account the inter-bin deformation fields are defined as:

$$\begin{aligned}\nabla_C^f\,\boldsymbol{x}_{r,c} &= \boldsymbol{x}_{r,c+1} - \boldsymbol{T}_C^{c\to c+1}\,\boldsymbol{x}_{r,c}\\ \nabla_R^f\,\boldsymbol{x}_{r,c} &= \boldsymbol{x}_{r+1,c} - \boldsymbol{T}_R^{r\to r+1}\,\boldsymbol{x}_{r,c}\\ \nabla_R^b\,\boldsymbol{x}_{r,c} &= \boldsymbol{x}_{r-1,c} - \boldsymbol{T}_R^{r\to r-1}\,\boldsymbol{x}_{r,c},\end{aligned} \tag{8}$$

with the following boundary conditions:

$$\begin{aligned}\nabla_C^f\boldsymbol{x}_{r,n_c} &= \boldsymbol{x}_{r,1} - \boldsymbol{T}_C^{n_c\to 1}\boldsymbol{x}_{r,n_c}\\ \nabla_R^f\boldsymbol{x}_{n_r,c} &= 0\\ \nabla_R^b\boldsymbol{x}_{1,c} &= 0,\end{aligned} \tag{9}$$

where $\boldsymbol{T}_C^{i\to j}$ and $\boldsymbol{T}_R^{i\to j}$ are interpolation matrices containing the non-rigid deformation fields resulting from the Demons registration of $\boldsymbol{x}_{R,i}$ to $\boldsymbol{x}_{R,j}$[29,31] and $\boldsymbol{x}_{i,C}$ to $\boldsymbol{x}_{j,C}$,[33] respectively. From the undersampled 5D motion-resolved data, $\boldsymbol{x}_{r,C}$ images were obtained by collapsing all cardiac bins, averaging the cardiac motion within each respiratory bin. Similarly, $\boldsymbol{x}_{R,c}$ images were derived by collapsing all respiratory bins to average the respiratory motion within each cardiac bin. However, due to the relatively high number of cardiac phases, significant undersampling remains within each respiratory-averaged cardiac bin. To mitigate this, a 4D CS-based reconstruction with low regularization

along the cardiac dimension was applied, which helps reduce undersampling artifacts and ensures accurate estimation of the deformation fields $\boldsymbol{T}_C$. Cardiac regularization weights were carefully selected to avoid compressing cardiac motion, as reported previously.[29]

The above optimization problem was solved with the alternating direction method of multipliers algorithm[35] using 10 iterations, $\rho = 0.06$, $\lambda_C = 0.005$, and $\lambda_R = 0.02$.

A Linux workstation with two 24-core CPUs (Intel Xeon Gold 6248R; Intel, Santa Clara, CA, USA), 1.5 TB of RAM, and an Nvidia RTX A6000 GPU (Nvidia, Santa Clara, CA, USA) was used to perform the offline reconstruction in Matlab R2021b (The MathWorks, Natick, MA, USA). The total image reconstruction time, including all data preparation steps, was recorded.

2.5 | Validation metrics

The end-expiratory respiratory phase of the 5D IRF and 5D FR data was reformatted into 2D SAX slices at the same spatial locations as the conventional 2D cine SAX images while preserving their intrinsic resolution (Figure 2D).

The quality of our IFR images was compared to that of the FR images without T_2 preparation and recovery time modules, as well as to conventional 2D cine SAX based on sharpness and contrast measurements. These measurements were performed for each subject in a mid-ventricular SAX view at end-diastole for sharpness assessment and during end-systole for blood pool-to-myocardium contrast assessment (Figure 3).

Image sharpness assessment involved manually placing points along the septal mid-left-ventricular blood pool-myocardium interface. A cubic Bézier curve was then fitted to interpolate through these points, with perpendicular lines evenly distributed along the curve. A sigmoid function f, defined as:

$$f(x, x_0, a_1, a_2, s) = a_2 + \frac{a_1 - a_2}{1 + 10^{(x_0 - x)s}}, \tag{10}$$

where x_0 is the center location, $a_1 = \lim_{x \to +\infty} f(x)$, $a_2 = \lim_{x \to -\infty} f(x)$, and s is the growth rate, was fitted to the intensity profile of each perpendicular line. This fit enabled the determination of the 10–90% rise distance (RD) of the sigmoid, expressed in millimeters as weighted by the pixel size (ps), and computed as:

$$\begin{aligned} \mathrm{RD} = (&f^{-1}(a_2 + 0.9(a_1 - a_2)) \\ &- f^{-1}(a_2 + 0.1(a_1 - a_2))) \times ps. \end{aligned} \tag{11}$$

The final RD score was computed as the mean of the RD scores of each perpendicular line at the blood-myocardium interface. A shorter RD indicates a more abrupt increase in intensity, signifying higher image sharpness. The blood-to-myocardium contrast ratio (CR) was calculated as the ratio between the average signal intensity in the blood pool (S_b) and in the myocardium (S_m). These two regions of interest were manually delineated at end-systole. Papillary muscles and trabeculations were not included in the segmentation of the blood pool. The CR was then computed as:

$$\mathrm{CR} = \frac{S_b - S_m}{S_m}. \tag{12}$$

Myocardial wall thickness (MWT) was measured at end-diastole using the same mid-ventricular SAX short-axis slice. The first two myocardial segments were positioned based on the orientation of the two-chamber

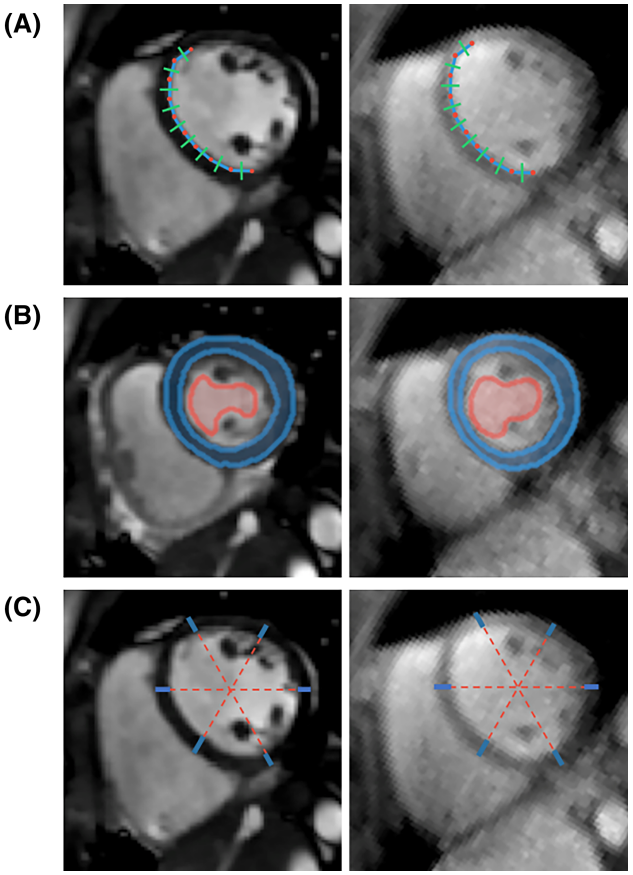

FIGURE 3 Image sharpness, contrast ratio, and myocardial wall thickness measurements. Blood-myocardium interface sharpness was assessed in a similar middle SAX slice for both 2D cine (left) and IFR (right) images at end-diastole (A). Blood-to-myocardium contrast was assessed in the same middle SAX slice for both 2D cine (left) and IFR (right) images at end-systole (B). Myocardial wall thickness was assessed in the same middle SAX slice for both 2D cine (left) and IFR (right) images at end-diastole (C).

view. The remaining four segments were evenly distributed around the ventricle at 60° intervals, using the center of the blood pool as the origin for angular measurements (Figure 3C). The final MWT value was calculated as the mean thickness measured at these six segments.

The endocardial contour was manually segmented on all SAX slices at end-diastole and end-systole for both our reformatted IFR and 2D cine SAX data using a segmentation software (cvi42, Circle Cardiovascular Imaging, Calgary, Canada). Papillary muscles and trabeculations were included in the blood-pool segmentation. End-diastolic (EDV) and end-systolic (ESV) left ventricle volumes were calculated from these segmentations, and the left ventricular ejection fraction (EF) was computed as:

$$\mathrm{EF} = \frac{(\mathrm{EDV} - \mathrm{ESV})}{\mathrm{EDV}} \times 100\%. \tag{13}$$

Volumes and EF from the 5D IRF and the 2D cine SAX images were compared using the intraclass correlation coefficient (ICC) with a 2,1 formula[36] and standard error of measurement (SEM). Furthermore, the measurement agreements between both sequences were assessed with correlation plots and Bland-Altman analysis.

Two-sided Student's t-tests were used for all metrics to assess differences, with $p < 0.05$ considered statistically significant.

3 | RESULTS

3.1 | Acquisition parameter optimization

The EPG simulations confirmed that longer acquisition times generally lead to a greater theoretical signal difference between the blood and myocardium (Figure 4). As expected, without the T_2 prep module, there was never a positive blood-myocardium contrast (Figure S1). It can be observed that no single parameter consistently provides the best theoretical D_{bm} across all acquisition times. Instead, the local maxima are composed of various parameter combinations. Therefore, the choice of parameters was taken as the optimal set for a specific acquisition time.

The optimal parameters for our IFR sequence with a fixed acquisition time of 5:00 min were therefore RF excitation angle 4°, 66 readouts per T_2 prep distributed in three radial interleaves of 22 readouts each, $TE_{T_2p} = 40$ ms and recovery time 160 ms. For the FR GRE acquisition, without the contrast-enhancing mechanisms, the optimal flip angle was 7° (Figure S2) for an acquisition of 2:40 min. The scan efficiency was 17% for the IFR sequence and 41% for the FR sequence.

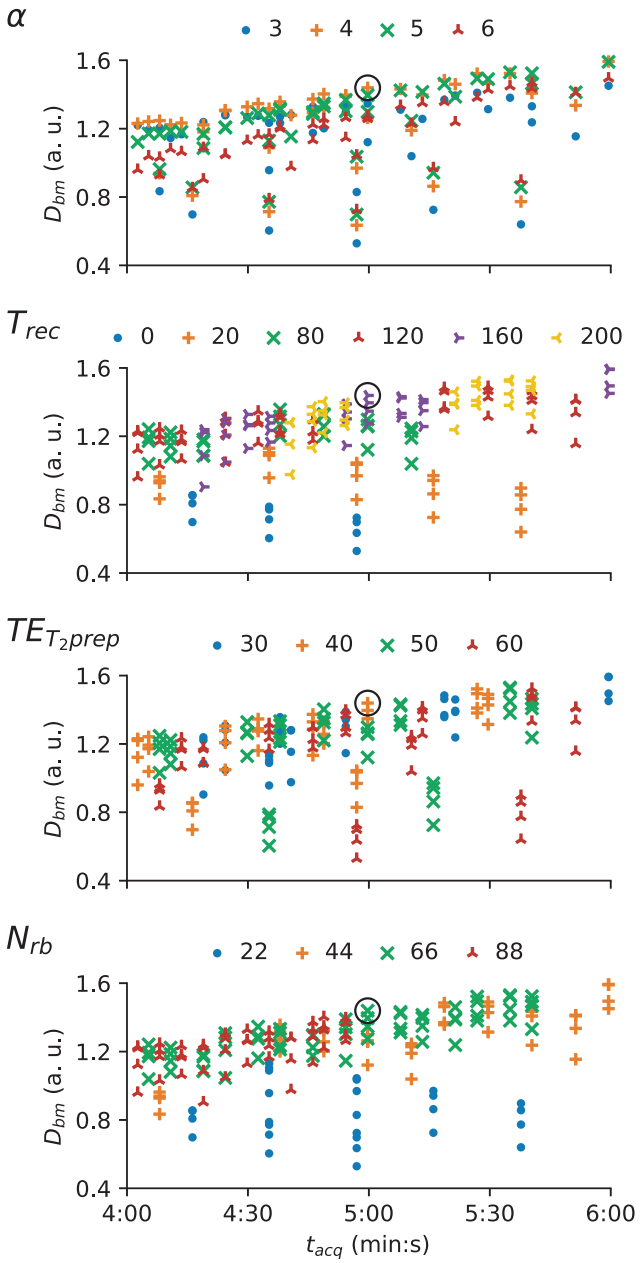

FIGURE 4 Theoretical blood-to-myocardium signal differences (D_{bm}) were computed by EPG simulation for selected subsets of the simulated parameters. The four plots display the same data points but use different combinations of colors and symbols to represent the parameter of interest of each plot. The x-axis shows the acquisition time (t_{acq}) for a total of 45,276 readouts. The selected optimal parameter combination is highlighted with a black circle.

The 5D and 2D images were successfully acquired in all participants. Visual inspection reveals that, in the absence of contrast-enhancing modules, the differentiation between the blood pool and myocardium is challenging in the native GRE sequence (Figure 5).

The sampling of the IFR acquisitions resulted in 3.02 ± 0.63% (range 1.25–5.25%), with only 50 out of 1360 motion

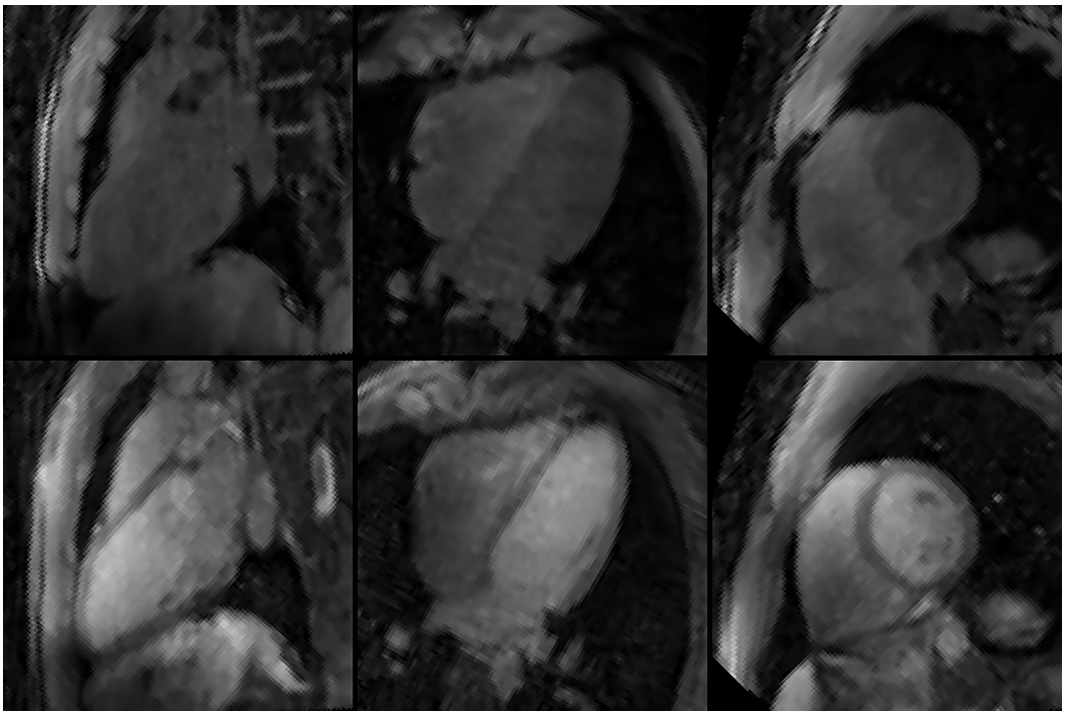

FIGURE 5 Comparison of free-running GRE acquisitions with and without contrast modules. Left 2-chamber, 4-chamber, and short-axis views of free-running GRE acquisitions at 3T with (bottom) and without (top) T_2 prep and recovery time modules. The images are displayed at the end-diastole and end-expiration phases.

state bins in total among all subjects falling below 2% Nyquist (Figure S3).

The clinical reference protocol for 2D cine acquisitions was completed in an average time of 8 min 12 s for the 16 healthy subjects and 9 min 34 s for the three patients, compared to the fixed 5 min for the IFR protocol.

The total image reconstruction time was approximately 4 h 30 min per 5D dataset.

3.2 | Image quality

The IFR images provided sufficient blood-myocardium contrast for left-ventricle segmentation with a contrast ratio (CR) of 0.569 ± 0.118. However, this contrast was lower than that of the 2D cine SAX images, which had a higher CR of 2.092 ± 0.741 ($p < 0.001$, Figure 6A). The contrast ratio for the FR images was the lowest, at -0.272 ± 0.029.

The left-ventricular blood-myocardium sharpness was the lowest for the FR images, with a rise distance (RD) of 4.550 ± 0.919, compared to the IFR images, which had an RD score of 3.766 ± 1.110. The 2D cine SAX images had the highest RD score of 2.741 ± 0.954 ($p < 0.001$, Figure 6B).

3.3 | Cardiac anatomy and function

The IFR images were reformatted to match the spatial location and orientation of the 2D SAX images (Figure 8). Certain details, such as the papillary muscles and trabeculations, are less discernible in IFR images compared to cine images, likely primarily due to the lower spatial resolution. Nevertheless, the distinction between the blood pool and the myocardium was sufficiently pronounced to enable effective segmentation of the left ventricle.

MWT was compared between the IFR and 2D cine methods. The MWT for the 2D paired two-sample Student's *t*-test revealed no statistically significant difference between the two methods ($p = 0.26$). Bland-Altman analysis demonstrated a bias of −0.24 mm, with limits of agreement ranging from −2.00 mm to +1.52 mm, indicating strong agreement between the two methods for MWT measurement (Figure 7).

Correlation plots (Figure 9) demonstrated high correlation between the 2D SAX and the proposed IFR images for EDV ($R^2 = 0.96$), ESV ($R^2 = 0.89$), and EF ($R^2 = 0.76$). Our subjects exhibited a wide range of EF, varying from 55% to 70%.

The Bland-Altman analyses (Figure 9) revealed a slight underestimation of both EDV and ESV values by the

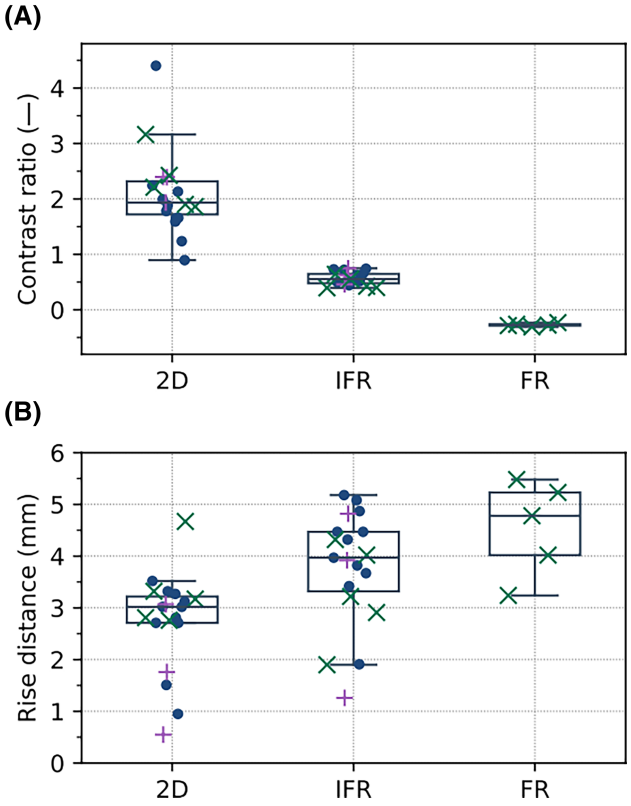

FIGURE 6 The contrast ratio (A) and rise distance (B) were computed on 2D SAX cine, the proposed interrupted free-running (IFR), and free-running (FR) images. Purple crosses represent patients, blue dots represent healthy volunteers, and green crosses indicate healthy volunteers who underwent both FR and IFR acquisitions.

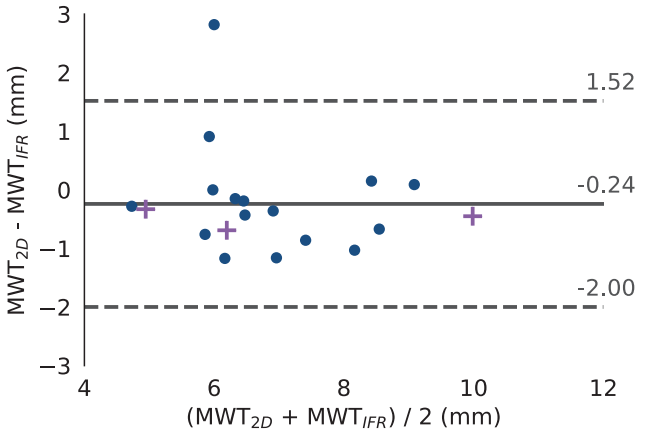

FIGURE 7 Bland-Altman plot comparing myocardial wall thickness (MWT) measurements between the IFR and 2D cine methods. Healthy volunteers and patients are represented by blue dots and purple crosses, respectively.

proposed method with a bias of −2.4 mL ($p = 0.12$) and −2.8 mL ($p = 0.01$), respectively. This underestimation for both EDV and ESV results in a low EF bias of 1.3% ($p = 0.03$). The 95% limits of agreement ranged from −15.0 to 10.2 mL for EDV, and from −11.2 to 5.6 mL for ESV, from −3.3 to 5.9% points for EF.

The proposed method exhibited high reproducibility compared to the routine 2D SAX method, as evidenced by ICC (and SEM) values of 0.98 (4.55 mL) for EDV, 0.96 (3.02 mL) for ESV, and 0.87 (1.66 mL) for EF.

4 | DISCUSSION

A fully automated framework for non-contrast 5D CMR at 3 T has been successfully developed and compared to the clinical standard 2D cine images. This framework demonstrated a high level of agreement in assessing left ventricular function across 16 healthy volunteers and three patients clinically referred for CMR scanning.

T_2 prep GRE techniques[37] at 3 T have so far primarily been used for static 3D whole-heart MR angiography,[16,18–20] which are not suited for functional assessment of the left ventricle. FR bSSFP techniques without T_2 prep[38] might be more time-efficient and provide similar blood myocardium contrast, but are likely to run into banding artifacts or SAR limitations at 3 T. Recently, an FR fast-interrupted steady-state (FISS) sequence has been proposed to obtain non-contrast 5D cardiac images at 3 T.[39] However, this technique has not yet been validated for assessing cardiac function, as its application was aimed at angiography alone. While FISS acquisitions at 3 T provide significant advantages in terms of image quality, the higher field strength introduces challenges such as increased susceptibility to artifacts and more pronounced off-resonance and B1 inhomogeneities. Addressing these drawbacks for functional imaging will require careful optimization of imaging protocols.

Our 5D IFR images exhibited a lower contrast ratio (0.57 ± 0.12) than the 2D cine images (2.09 ± 0.74) and contrast-enhanced GRE FR images reported in the literature with a CR of 1.5 ± 0.3.[11] Despite the lower contrast ratio, our method demonstrated high robustness as indicated by the lower CR standard deviation and the ease of analysis with a commercial software package. Indeed, while the overall quality of the proposed images was lower than that of the 2D cine images, manual segmentation of the left ventricle was straightforward and demonstrated very high agreement between the proposed method and the conventional 2D cine method for evaluating cardiac anatomy (ICC > 0.96 for EDV and ESV) and cardiac function (ICC > 0.87). The reported limits of agreements, ranging from −15.0 to 10.2 mL for EDV, −11.2 to 5.6 mL for ESV, and −3.3 to 5.9 % for EF, are comparable to previously reported scores in the literature for intra-expert variability in left-ventricle segmentation on 2D SAX cine images:

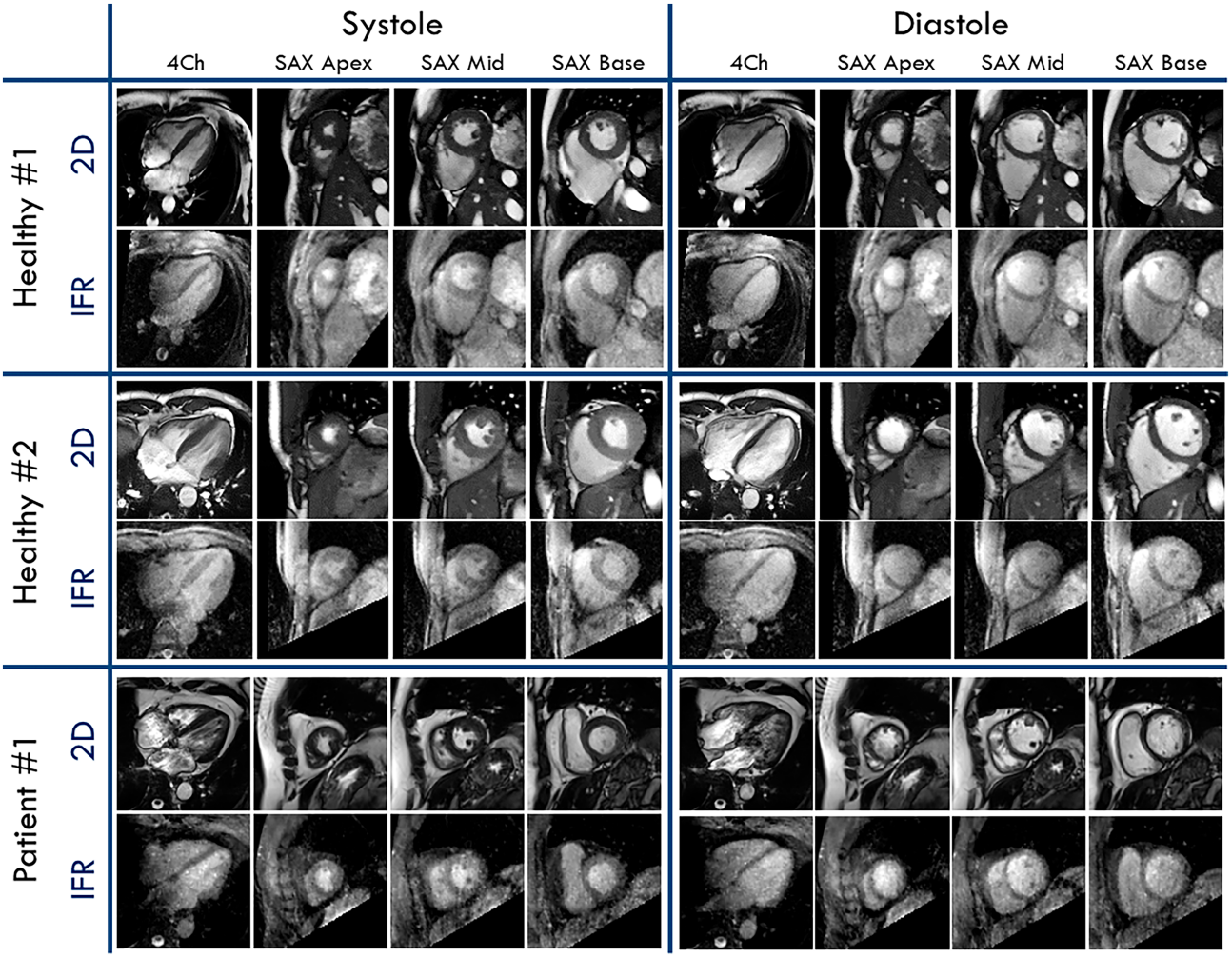

FIGURE 8 Qualitative comparison between 2D routine SAX cine and orientation-matched proposed IFR images in three subjects at end-systolic and end-diastolic phases. Shown are matching four-chamber (4Ch) as well as apical, mid-ventricular, and basal short-axis (SAX) slices. A slight variance in slice anatomical location can be noted due to the acquisition of 2D cine during breath-holds, while the reformatted images were extracted from the end-expiratory phase of the free-breathing acquisition. Shown are two healthy volunteers and a patient diagnosed with chronic ischemic heart disease.

using the same segmentation software as in our study, Zange et al. reported limits of agreement of −7.9 to 11.7 mL for EDV, −6.7 to 8.0 mL for ESV, and −4.9 to 4.6% for EF.[40] The proposed sequence was evaluated in participants without pathologically low EFs (< 50%) or arrhythmia. While low EF itself should not pose a problem for the technique, the method will likely need to be optimized and characterized in patients with arrhythmias.

It should be noted that comparing left-ventricular volumes derived from free-running methods to those obtained from 2D acquisitions is inherently challenging because of their physiological differences.[41] The IFR acquisition occurs during free breathing with an oscillating respiratory state, whereas the 2D SAX cine acquisition is performed in a breath-held state. The reformatting of the 5D IFR images into SAX views was based on the absolute scanner position of the 2D cine images. Consequently, slight variations in slice anatomical locations will lead to differences in the segmented areas between the two methods. This bias might explain the slight underestimation of EDV (−2.4 ml) and ESV (−2.8 ml) volumes while maintaining an EF bias of 1.3%.

The proposed IFR method has a lower scan efficiency (i.e. the ratio of the time spent reading out signal to the total scan time) than previously demonstrated bSSFP-based FR approaches due to the presence of T_2 prep and recovery time modules. By leveraging EPG simulations, we ensured an optimal contrast for a 5-min acquisition time, which is comparable to that used for bSSFP-based FR at 1.5 T.[9] These acquisition times should be considered in the context of 2D cine acquisitions. Such approaches exhibit a low scan efficiency due to the

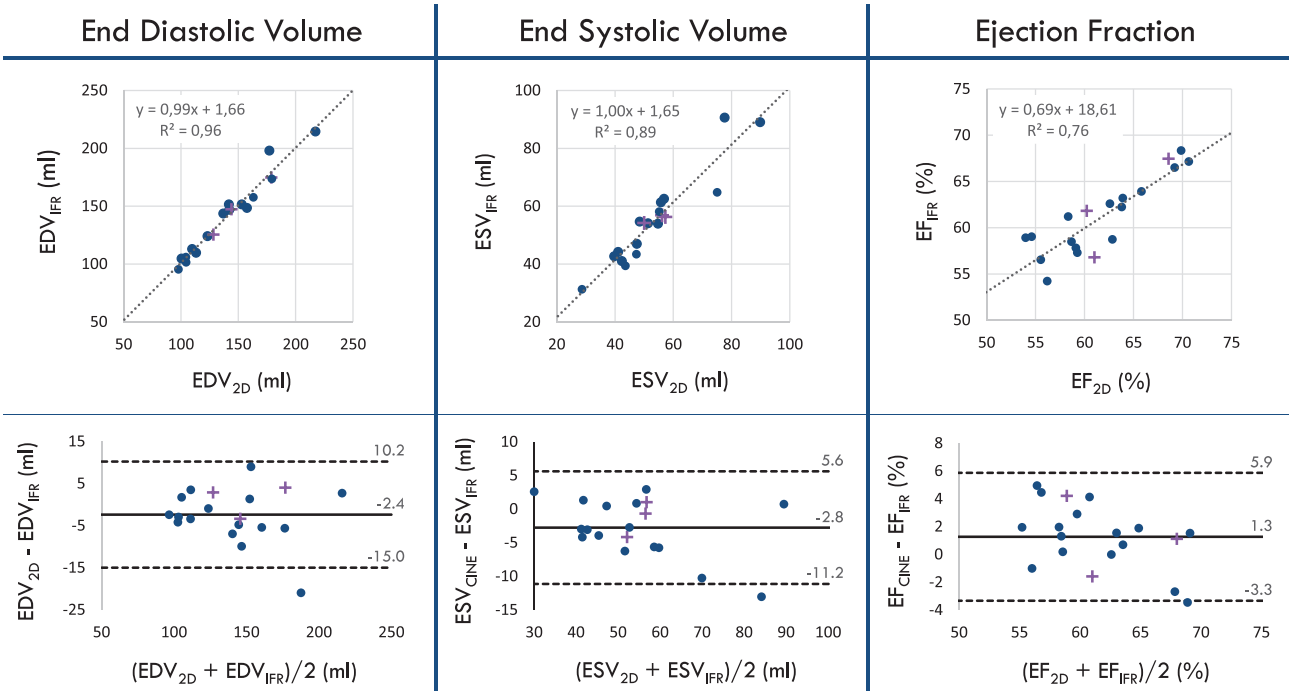

FIGURE 9 Correlation plots (top) and Bland-Altman analysis (bottom) between the 2D SAX cine and the proposed IFR method for the end-diastolic left ventricle volume (EDV), end-systolic left ventricle volume (ESV), and left ventricle ejection fraction (EF). Healthy volunteers and patients are represented by blue dots and purple crosses, respectively. In the Bland-Altman analyses, the central lines indicate the mean difference, and the dashed lines indicate the limits of agreement.

time-consuming and proficiency-demanding planning of double oblique cardiac views and the pauses between breath-holds. The scan time for a comprehensive assessment of left ventricular cardiac function and anatomy using 2D cine MRI methods typically lasts up to 10 min for patients. Moreover, the total acquisition time for a complete cardiac evaluation with 2D cine imaging is directly related to the number of desired cardiac views, while no additional views can be created afterwards, for example, if the atrial volumes become of interest after the scan has ended. In contrast, the IFR method requires only a single acquisition, which provides isotropic 5D images that can be reformatted into any desired view retrospectively. Furthermore, since it only requires the placement of a single 3D volume in the standard cardinal planes around the heart, 5D IFR allows cardiac cine imaging to be performed by any operator, not just by those with specialized training in cardiac MRI.

The addition of T_2 prep and recovery time modules prevented our acquisition from being fully self-gated, as the SI sampling was insufficient to accurately capture cardiac motion. Therefore, cardiac binning was achieved using a pulse oximeter. This non-invasive, easy-to-use device can often be employed at 3 T when reliable ECG triggering is not achievable.[42] This limitation could be addressed in the future by either filtering out unwanted signal variations among the SI projections caused by the T_2 prep module using algorithms such as SSA-FARY[43] or by implementing a pilot-tone navigation system, which would further simplify the acquisition workflow by minimizing the need for external gating.[44–46] The sampling pattern of the proposed IFR framework resulted in sufficient sampling per motion state[29] for the compressed-sensing reconstruction to achieve high image quality in all of the motion states.

An additional potential limitation of our proposed method is the reconstruction time. High-performance computing infrastructure is crucial for CS-based reconstruction of 5D images. Integrating both cardiac and respiratory inter-bin deformation fields into the CS-based reconstruction allows for the use of larger regularization weights without introducing motion blur and reduces sensitivity to user-defined parameters. However, this also increases the computational burden, leading to delays in the availability of imaging results and potentially impacting clinical workflow efficiency. Finally, the relatively low spatial resolution of $(1.96\ \text{mm})^3$ used in this study limits the visualization of finer anatomical structures and details, restricting our validation to left ventricular function assessment.

The proposed method is a step toward non-contrast CMR acquisitions, which would be particularly beneficial for patients with contraindications to contrast agents,

such as renal impairment or allergies, or when minimizing invasive procedures and enhancing patient comfort while reducing scan costs is a priority. However, it is recognized that many clinical studies, particularly those involving ischemic heart disease, will still rely on contrast agents for essential applications, such as perfusion imaging, late enhancement, and angiography, where enhanced tissue differentiation is critical.

Importantly, our contribution goes beyond proposing only an acquisition scheme; we introduce a flexible framework designed to determine the optimal parameters for any type of interrupted free-running sequence. The EPG simulations demonstrated that no single acquisition parameter consistently provides the best theoretical D_{bm} across all durations. The parameters cannot be optimized separately; they must be optimized together. This framework is inherently adaptable to higher-resolution imaging or other contrast mechanisms (inversion recovery, mapping, flow), etc.). For instance, if a higher spatial resolution is desired, the same EPG simulations as those presented in this study could be used. The only adjustment required would be the number of readouts, and consequently, the acquisition time, to maintain an adequate Nyquist sampling percentage. Theoretically, acquiring contrast-agent-free 5D images at a resolution of $(1.1\ \text{mm})^3$ would extend the scan time to approximately 14 min. Such an acquisition would enable more detailed anatomical studies, including the visualization of coronary arteries, and enhance functional evaluations, making the framework highly valuable for clinical practice. In this study, the EPG simulation optimizations were largely based on the sequence timing and relaxation mechanisms and did not take blood flow, magnetic field inhomogeneities, or motion into account, although these are expected to have a small effect in this non-selective 3D GRE acquisition. Furthermore, we used EPG simulations to optimize the contrast for a fixed total number of readouts within a 5-min acquisition time. Future studies could explore the trade-off between longer acquisition times, optimal theoretical contrast, and maximal sampling percentage.

5 | CONCLUSION

This study introduced a novel automated framework for non-contrast 5D CMR at 3 T, designed for a 5-min acquisition and demonstrating strong concordance with conventional 2D cine imaging in evaluating left ventricular function across both healthy volunteers and patients. While the absence of contrast agent injection offers significant advantages in scenarios where they are contraindicated or when minimizing injections is a priority, it comes at the cost of reduced scan efficiency. Specifically, the proposed framework achieves a 17% scan efficiency compared to free-running acquisitions with continuous data capture, which typically exhibit a scan efficiency of 41%. Although the framework yields images with lower contrast than conventional 2D cine techniques, it offers robust performance and straightforward analyses, with high equivalent cardiac function measurements to those of conventional techniques. The flexibility of the proposed framework allows it to be adapted for higher-resolution imaging or other types of interrupted free-running sequences, potentially broadening its clinical applications. The proposed framework thus promises to enhance the efficiency of whole-heart imaging, potentially streamlining workflows and enabling comprehensive cardiac assessments from a single acquisition.

CONFLICTS OF INTEREST STATEMENT

We acknowledge that the co-author Matthias Stuber receives patent royalties for the adiabatic T_2 prep used in this study (US Patents US7375520B2 & US7787930B2). All other authors declare no competing interests.

ORCID

Augustin C. Ogier https://orcid.org/0000-0001-9178-9964
Isabel Montón Quesada https://orcid.org/0009-0009-0585-4391
Xavier Sieber https://orcid.org/0009-0002-4655-1265
Pauline Calarnou https://orcid.org/0000-0003-3273-460X
Jean-Baptiste Ledoux https://orcid.org/0000-0003-0447-5073
Bastien Milani https://orcid.org/0000-0002-2410-2744
Panagiotis Antiochos https://orcid.org/0000-0001-8466-7360
Juerg Schwitter https://orcid.org/0000-0002-9966-6149
Christopher W. Roy https://orcid.org/0000-0002-3111-8840
Jérôme Yerly https://orcid.org/0000-0003-4347-8613
Matthias Stuber https://orcid.org/0000-0001-9843-2028
Ruud B. van Heeswijk https://orcid.org/0000-0001-5028-4521

REFERENCES

1. GBD 2017. Causes of Death Collaborators. Global, regional, and national age-sex-specific mortality for 282 causes of death in 195 countries and territories, 1980–2017: A systematic analysis for the global burden of disease study 2017. *The Lancet*. 2018;392:1736-1788. doi:10.1016/S0140-6736(18)32203-7
2. Bolognese L, Neskovic AN, Parodi G, et al. Left ventricular remodeling after primary coronary angioplasty: Patterns of left ventricular dilation and long-term prognostic implications. *Circulation*. 2002;106:2351-2357. doi:10.1161/01.CIR.0000036014.90197.FA

3. Kramer CM, Barkhausen J, Bucciarelli-Ducci C, Flamm SD, Kim RJ, Nagel E. Standardized cardiovascular magnetic resonance imaging (CMR) protocols: 2020 update. *Journal of Cardiovascular Magnetic Resonance.* 2020;22:17. doi:10.1186/s12968-020-00607-1
4. Von Knobelsdorff-Brenkenhoff F, Schulz-Menger J. Cardiovascular magnetic resonance in the guidelines of the European society of cardiology: A comprehensive summary and update. *Journal of Cardiovascular Magnetic Resonance.* 2023;25:42. doi:10.1186/s12968-023-00950-z
5. Pang J, Sharif B, Fan Z, et al. ECG and navigator-free four-dimensional whole-heart coronary MRA for simultaneous visualization of cardiac anatomy and function. *Magn Reson Med.* 2014;72:1208-1217. doi:10.1002/mrm.25450
6. Coppo S, Piccini D, Bonanno G, et al. Free-running 4D whole-heart self-navigated golden angle MRI: Initial results. *Magn Reson Med.* 2015;74:1306-1316. doi:10.1002/mrm.25523
7. Larson AC, Kellman P, Arai A, et al. Preliminary investigation of respiratory self-gating for free-breathing segmented cine MRI. *Magn Reson Med.* 2005;53:159-168. doi:10.1002/mrm.20331
8. Larson AC, White RD, Laub G, McVeigh ER, Li D, Simonetti OP. Self-gated cardiac cine MRI. *Magn Reson Med.* 2004;51:93-102. doi:10.1002/mrm.10664
9. Di Sopra L, Piccini D, Coppo S, Stuber M, Yerly J. An automated approach to fully self-gated free-running cardiac and respiratory motion-resolved 5D whole-heart MRI. *Magn Reson Med.* 2019;82:2118-2132. doi:10.1002/mrm.27898
10. Tyler D, Hudsmith L, Petersen S, et al. Cardiac cine MR-imaging at 3T: FLASH vs SSFP. *J Cardiovasc Magn Reson*. 2006;8:709-715. doi:10.1080/10976640600723797
11. Ishida M, Yerly J, Ito H, et al. Optimal protocol for contrast-enhanced free-running 5D whole-heart coronary MR angiography at 3T. *MRMS.* 2024;23:225-237. doi:10.2463/mrms.tn.2022-0086
12. Mathur M, Jones JR, Weinreb JC. Gadolinium deposition and nephrogenic systemic fibrosis: A radiologist's primer. *RadioGraphics.* 2020;40:153-162. doi:10.1148/rg.2020190110
13. McDonald RJ, Levine D, Weinreb J, et al. Gadolinium retention: A research roadmap from the 2018 NIH/ACR/RSNA workshop on gadolinium chelates. *Radiology.* 2018;289:517-534. doi:10.1148/radiol.2018181151
14. Brittain JH, Hu BS, Wright GA, Meyer CH, Macovski A, Nishimura DG. Coronary angiography with magnetization-prepared T_2 contrast. *Magn Reson Med.* 1995;33:689-696. doi:10.1002/mrm.1910330515
15. Botnar RM, Stuber M, Danias PG, Kissinger KV, Manning WJ. Improved coronary artery definition with T2-weighted, free-breathing, three-dimensional coronary MRA. *Circulation.* 1999;99:3139-3148. doi:10.1161/01.CIR.99.24.3139
16. Coristine AJ, Van Heeswijk RB, Stuber M. Improved fat signal suppression for coronary MRA at 3T using a water-selective adiabatic T2-prep technique. *J Cardiovasc Magn Reson*. 2013;15:O5. doi:10.1186/1532-429X-15-S1-O5
17. Monney P, Piccini D, Rutz T, et al. Single centre experience of the application of self navigated 3D whole heart cardiovascular magnetic resonance for the assessment of cardiac anatomy in congenital heart disease. *J Cardiovasc Magn Reson*. 2015;17:55. doi:10.1186/s12968-015-0156-7
18. Coristine AJ, Chaptinel J, Ginami G, et al. Improved respiratory self-navigation for 3D radial acquisitions through the use of a pencil-beam 2D-T_2 -prep for free-breathing, whole-heart coronary MRA. *Magn Reson Med.* 2018;79:1293-1303. doi:10.1002/mrm.26764
19. Milotta G, Ginami G, Cruz G, Neji R, Prieto C, Botnar RM. Simultaneous 3D whole-heart bright-blood and black blood imaging for cardiovascular anatomy and wall assessment with interleaved T_2 prep-IR. *Magn Reson Med.* 2019;82:312-325. doi:10.1002/mrm.27734
20. Isaak A, Mesropyan N, Hart C, et al. Non-contrast free-breathing 3D cardiovascular magnetic resonance angiography using REACT (relaxation-enhanced angiography without contrast) compared to contrast-enhanced steady-state magnetic resonance angiography in complex pediatric congenital heart disease at 3T. *J Cardiovasc Magn Reson*. 2022;24:55. doi:10.1186/s12968-022-00895-9
21. Nezafat R, Stuber M, Ouwerkerk R, Gharib AM, Desai MY, Pettigrew RI. *B1* -insensitive *T2* preparation for improved coronary magnetic resonance angiography at 3T. *Magn Reson Med.* 2006;55:858-864. doi:10.1002/mrm.20835
22. Sieber X, Romanin L, Bastiaansen JAM, et al. A flexible framework for the design and optimization of water-excitation RF pulses using B-spline interpolation. *Magn Reson Med.* 2024;1-15. doi:10.1002/mrm.30390
23. Piccini D, Littmann A, Nielles-Vallespin S, Zenge MO. Spiral phyllotaxis: The natural way to construct a 3D radial trajectory in MRI. *Magn Reson Med.* 2011;66:1049-1056. doi:10.1002/mrm.22898
24. Malik SJ, Padormo F, Price AN, Hajnal JV. Spatially resolved extended phase graphs: Modeling and design of multipulse sequences with parallel transmission. *Magn Reson Med.* 2012;68:1481-1494. doi:10.1002/mrm.24153
25. Stanisz GJ, Odrobina EE, Pun J, et al. T1, T2 relaxation and magnetization transfer in tissue at 3T. *Magn Reson Med.* 2005;54:507-512. doi:10.1002/mrm.20605
26. Vincenti G, Monney P, Chaptinel J, et al. Compressed sensing single–breath-hold CMR for fast quantification of LV function, volumes, and mass. *JACC Cardiovasc Imaging*. 2014;7:882-892. doi:10.1016/j.jcmg.2014.04.016
27. Liu J, Rapin J, Chang TC, et al. Dynamic cardiac MRI reconstruction with weighted redundant Haar wavelets. *International Society for Magnetic Resonance in Medicine (ISMRM)*; 2012 Abstract 4249.
28. Bishop SM, Ercole A. Multi-scale peak and trough detection optimised for periodic and quasi-periodic neuroscience data. *Intracranial Pressure & Neuromonitoring XVI.* 2018;126:189-195. doi:10.1007/978-3-319-65798-1_39
29. Yerly J, Roy CW, Milani B, Eyre K, Raifee MJ, Stuber M. High on sparsity: Interbin compensation of cardiac motion for improved assessment of left-ventricular function using 5D whole-heart MRI. *Magn Reson Med.* 2025;93:975-992. doi:10.1002/mrm.30323
30. Phair A, Cruz G, Qi H, Botnar RM, Prieto C. Free-running 3D whole-heart T1 and T2 mapping and cine MRI using low-rank reconstruction with non-rigid cardiac motion correction. *Magn Reson Med.* 2023;89:217-232. doi:10.58530/2022/1005

31. Milani B, Roy C, Ledoux JB, et al. Improving 3D-CINE tTV-regularized whole-heart MRI reconstruction. *MedRxiv.* 2024. doi:10.1101/2024.02.22.24302997
32. Asif MS, Hamilton L, Brummer M, Romberg J. Motion-adaptive spatio-temporal regularization for accelerated dynamic MRI. *Magn Reson Med.* 2013;70:800-812. doi:10.1002/mrm.24524
33. Roy CW, Milani B, Yerly J, et al. Intra-bin correction and inter-bin compensation of respiratory motion in free-running five-dimensional whole-heart magnetic resonance imaging. *J Cardiovasc Magn Reson*. 2024;26:101037. doi:10.1016/j.jocmr.2024.101037
34. Feng L, Coppo S, Piccini D, et al. 5D whole-heart sparse MRI. *Magn Reson Med.* 2018;79:826-838. doi:10.1002/mrm.26745
35. Boyd S, Parikh N, Chu E, Peleato B, Eckstein J. Distributed optimization and statistical learning via the alternating direction method of multipliers. *FNT in Machine Learning.* 2010;3:1-122. doi:10.1561/2200000016
36. Shrout PE, Fleiss JL. Intraclass correlations: Uses in assessing rater reliability. *Psychol Bull*. 1979;86:420-428. doi:10.1037/0033-2909.86.2.420
37. Parrish T, Hu X. A new T_2 preparation technique for ultrafast gradient-echo sequence. *Magn Reson Med.* 1994;32:652-657. doi:10.1002/mrm.1910320515
38. Küstner T, Bustin A, Jaubert O, et al. Fully self-gated free-running 3D Cartesian cardiac CINE with isotropic whole-heart coverage in less than 2 min. *NMR Biomed*. 2021;34:e4409. doi:10.1002/nbm.4409
39. Bastiaansen JAM, Piccini D, Di Sopra L, et al. Natively fat-suppressed 5D whole-heart MRI with a radial free-running fast-interrupted steady-state (FISS) sequence at 1.5T and 3T. *Magn Reson Med.* 2020;83:45-55. doi:10.1002/mrm.27942
40. Zange L, Muehlberg F, Blaszczyk E, et al. Quantification in cardiovascular magnetic resonance: agreement of software from three different vendors on assessment of left ventricular function, 2D flow and parametric mapping. *J Cardiovasc Magn Reson*. 2019;21:12. doi:10.1186/s12968-019-0522-y
41. Van Heeswijk RB, Bonanno G, Coppo S, Coristine A, Kober T, Stuber M. Motion compensation strategies in magnetic resonance imaging. *Crit Rev Biomed Eng.* 2012;40:99-119. doi:10.1615/CritRevBiomedEng.v40.i2.20
42. Krug JW, Rose G. Magnetohydrodynamic distortions of the ECG in different MR scanner configurations. *Comput. Cardiol.* 2011;38:769-772.
43. Rosenzweig S, Scholand N, Holme HCM, Uecker M. Cardiac and respiratory self-gating in radial MRI using an adapted singular spectrum analysis (SSA-FARY). *IEEE Trans Med Imaging.* 2020;39:3029-3041. doi:10.1109/TMI.2020.2985994
44. Ludwig J, Speier P, Seifert F, Schaeffter T, Kolbitsch C. Pilot tone–based motion correction for prospective respiratory compensated cardiac cine MRI. *Magn Reson Med.* 2021;85:2403-2416. doi:10.1002/mrm.28580
45. Ludwig J, Kerkering KM, Speier P, Schaeffter T, Kolbitsch C. Pilot tone-based prospective correction of respiratory motion for free-breathing myocardial T1 mapping. *Magn Reson Mater Phy.* 2022;36:135-150. doi:10.1007/s10334-022-01032-4
46. Falcão MBL, Di Sopra L, Ma L, et al. Pilot tone navigation for respiratory and cardiac motion-resolved free-running 5D flow MRI. *Magn Reson Med.* 2022;87:718-732. doi:10.1002/mrm.29023

SUPPORTING INFORMATION

Additional supporting information may be found in the online version of the article at the publisher's website.

Figure S1. Theoretical blood-to-myocardium signal differences (D_{bm}) were computed by EPG simulation with no T_2 prep module for selected subsets of simulated parameters. The three plots display the same data points but use different combinations of colors and symbols to represent the parameter of interest of each plot. The x-axis shows the acquisition time (t_{acq}) for a total of 45,276 readouts. α = RF excitation angle, T_{rec} = recovery time duration, N_{rb} = number of readouts per T_2 prep.

Figure S2. EPG simulations of the signal and contrast in the heart for a continuous free-running GRE sequence without T_2 prep or recovery time modules. The contrast is now almost purely driven by the T_1 relaxation time. The maximal contrast difference occurs at a flip angle of 7°, where the myocardium appears brighter than the blood pool.

Figure S3. A) Heatmap representation of the Nyquist percentage per unique motion state bin, computed for one subject in the study. B) Histogram of the Nyquist percentage for all 1360 motion state bins across all subjects in the study.

How to cite this article: Ogier AC, Montón Quesada I, Sieber X, et al. Free-running 5D whole-heart MRI for isotropic cardiac function measurements at 3T without contrast agents. *Magn Reson Med*. 2025;1-15. doi: 10.1002/mrm.30469

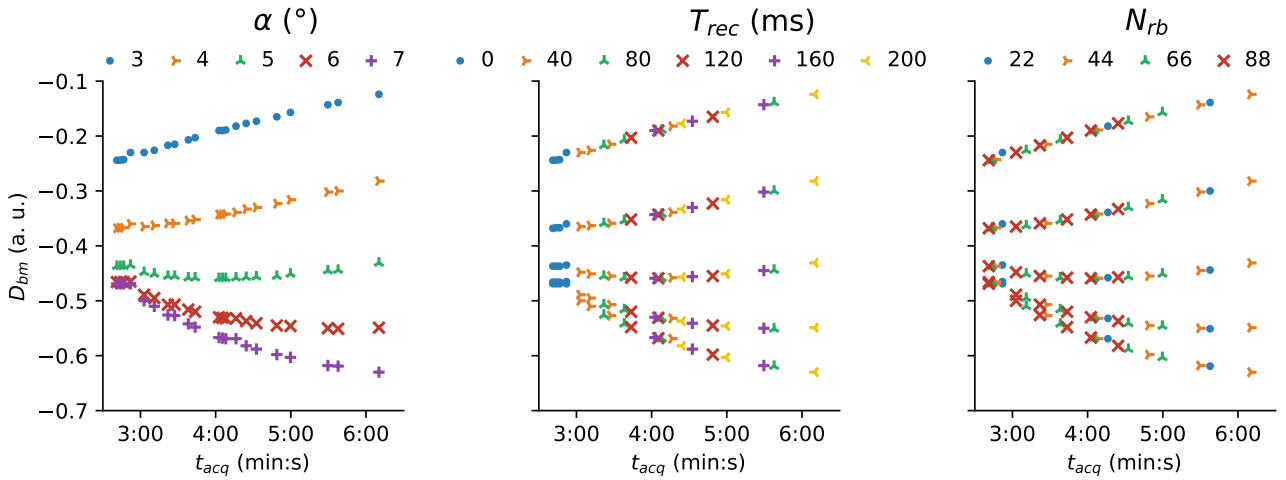

FIGURE S1 Theoretical blood-to-myocardium signal differences (D_{bm}) computed by EPG simulation with no T_2prep module for selected subsets of simulated parameters. The three plots display the same data points but use different combinations of colors and symbols to represent the parameter of interest of each plot. The x-axis shows the acquisition time (t_{acq}) for a total of 45,276 readouts. α = RF excitation angle, T_{rec} = recovery time duration, N_{rb} = number of readouts per T_2prep.

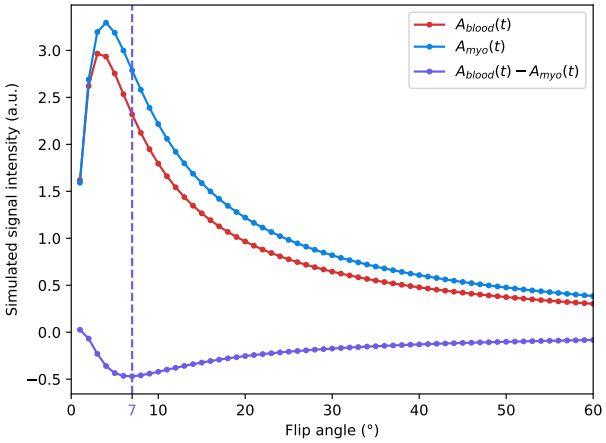

FIGURE S2 EPG simulations of the signal and contrast in the heart for a continuous free-running GRE sequence without T_2prep or recovery time modules. The contrast is now almost purely driven by the T_1 relaxation time. The maximal contrast difference occurs at a flip angle of 7°, where the myocardium appears brighter than the blood pool.

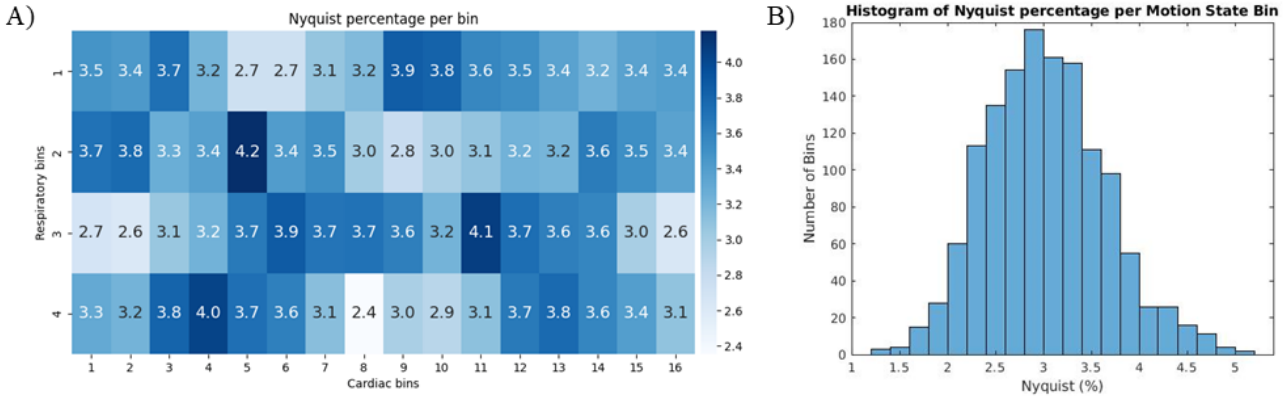

FIGURE S3 A) Heatmap representation of the Nyquist percentage per unique motion state bin, computed for one subject in the study. B) Histogram of the Nyquist percentage for all 1360 motion state bins across all subjects in the study.